UO'K: 620.9:628.16:536.2:532.546 https://doi.org/10.70769/2181-4732.ITJ.2026-2.16

KAPILLYAR TUZILMALI G'OVAK MUHIT YORDAMIDA QUYOSH CHUCHUTGICHINING SAMARADORLIGINI OSHIRISH: UCH O'LCHOVLI SONLI TAHLIL VA EKSPERIMENTAL TASDIQLASH

Asqarov Murodbek – mustaqil izlanuvchi, E-mail: asqarov.murodbek@gmail.com,
ORCID: 0009-0003-5182-7630, Science ID: MXR-0426-0217
Raximov Nurbek Zokirovich – assistent, E-mail: rahimov1570@gmail.com,
ORCID ID 0000-0002-5194-5843, Science ID: MQD-0626-0103

Qarshi davlat texnika universiteti, Qarshi, O'zbekiston

Annotatsiya. *Ushbu tadqiqot kapillyar tuzilmali g'ovak membrana bilan integratsiyalangan quyosh energiyasida ishlovchi chuchutish qurilmasi uchun kompleks uch o'lchovli sonli modelni taqdim etadi. Boshqaruvchi tenglamalar, jumladan, issiqlik almashinuvi, kapillyar ta'sirida yuzaga keluvchi massa almashinuvi, Darcy-Brinkman impuls tenglamalari hamda Hertz-Knudsen formulasi asosidagi fazalararo bug'lanish jarayonlari chekli hajmlar usuli (FVM) yordamida* $6,4 \times 10^6$ *nazorat hajmlaridan iborat to'rda bir vaqtda yechildi va ikkinchi tartibli* L^2 *xatolik 0,28% ga erishildi. G'ovaklik (φ=0,20-0,90) va kapillyar diametri (d=10-200 mkm) bo'yicha parametrik optimallashtirish natijasida φ=0,65 va d=35 mkm qiymatlarda eng yaxshi ekanligi aniqlanib, maksimal issiqlik samaradorligi η=83,7 ± 2,2% hamda kunlik chuchuk suv ishlab chiqarish* $14,8 \pm 0,8$ *kg/m²·kun ga yetgani qayd etildi (1000 W/m² quyosh nurlanishi sharoitida), bu an'anaviy tekis absorberlarga nisbatan 97,9 % ga yuqori ko'rsatkichni tashkil etadi.*

Kapillyar strukturali g'ovak membrana (CPM) asosidagi quyosh chuchitgich qurilmasi Darcy-Brinkman-Forchheimer 3D matematik model yordamida tadqiq etildi. Issiqlik uzatish, massa almashish va kapillyar momentum tenglamalari bir vaqtda yechildi. Adaptiv chekli hajmlar metodi (FVM) $6,4 \times 10^6$ *boshqaruv hajmli tarmoqda ikkinchi tartibli aniqlikda amalga oshirildi. G'ovaklilik φ = 0,20–0,90 va kapillyar diametr d=10-200 μm oralig'ida parametrik optimallashtirish o'tkazildi. Model natijalari laboratoriya tajribalari bilan taqqoslanib tasdiqlandi. Bug'lanish kinetikasi Hertz-Knudsen tenglamasi orqali, tuz transporti esa reaktiv adveksiya-diffuziya tenglamasi orqali modellashtirildi.*

Optimal konfiguratsiya φ=0,65 va d=35 μm bo'lganda issiqlik samaradorligi η=83,7 ± 2,2% ga, kunlik hosildorlik esa $14,8 \pm 0,8\, kg/m^2 kun$ *ga yetdi. Bu ko'rsatkichlar an'anaviy va yassi qurilmaga nisbatan mos ravishda 97,9 % va 185 % yuqori bo'ldi. Sonli model tajriba ma'lumotlari bilan MAE=1,9% va* $R^2=0,9974$ *aniqlikda mos keldi. Kapillyar oqim konsentratsiya polyarizatsiyasini 44,3% ga kamaytirdi va erigan moddalarni 62 ± 12 mg/L ga tushirdi, bu WHO standartidan 8 baravar past. Optimallik cho'qqisi φ≈0,645 da irradiance qiymatidan mustaqil ravishda saqlanib qoldi. Kapillyar qurilma an'anaviy absorberga nisbatan tuz qoldig'ini 480 dan 62 mg/L ga kamaytirib, suv tozaligini tubdan yaxshiladi.*

Kalit so'zlar: *quyosh chuchutish, kapillyar tuzilmali g'ovak membrana, chekli hajmlar usuli, issiqlik samaradorligi, kapillyar chiqish, kontsentratsion polaryatsiya, Hertz-Knudsen bo'yicha bug'lanish.*

УДК: 620.9:628.16:536.2:532.546

ПОВЫШЕНИЕ ЭФФЕКТИВНОСТИ СОЛНЕЧНОГО ОПРЕСНИТЕЛЯ С ИСПОЛЬЗОВАНИЕМ КАПИЛЛЯРНО-СТРУКТУРИРОВАННОЙ ПОРИСТОЙ СРЕДЫ: ТРЁХМЕРНЫЙ ЧИСЛЕННЫЙ АНАЛИЗ И ЭКСПЕРИМЕНТАЛЬНАЯ ВАЛИДАЦИЯ

Аскаров Муродбек – самостоятельный соискатель
Рахимов Нурбек Зокирович – ассистент

Каршинский государственный технический университет, г. Карши, Узбекистан

2026-yil 2(62)-son
2026 volume 62, number 2
Том 62 № 2, 2026
ISSN 2181-4732
E-ISSN 2181-4015

Аннотация. *Данное исследование представляет собой комплексную трёхмерную сопряжённую численную модель солнечного опреснительного устройства, включающего капиллярно-структурированную пористую мембрану (CPM). Управляющие уравнения, охватывающие сопряжённый теплообмен, капиллярно-обусловленный массоперенос, уравнения импульса Дарси-Бринкманна и межфазное испарение по формулировке Герца-Кнудсена, решаются совместно с использованием адаптивного метода конечных объёмов (FVM) на сетке, содержащей 6,4×10^6 контрольных объёмов, с достижением ошибки второго порядка L^2, равной 0,28%. Параметрическая оптимизация по пористости (φ=0,20-0,90) и диаметру капилляров (d=10-200 мкм) позволила определить глобальный оптимум при φ=0,65 и d=35 мкм, обеспечивающий максимальную тепловую эффективность η=83,7 ± 2,2% и суточную производительность по пресной воде 14,8 ± 0,8 кг/$м^2$·сут при солнечной радиации 1000 Вт/$м^2$, что на 97.9% превышает показатели традиционных плоских абсорберов.*

Солнечная опреснительная установка на основе капиллярно-структурированной пористой мембраны (CPM) была исследована с использованием трёхмерной математической модели, основанной на уравнениях Дарси–Бринкмана–Форхгеймера. Уравнения теплопереноса, массопереноса и импульса с учётом капиллярных сил решались совместно в связанной постановке. Адаптивный метод конечных объёмов (FVM) был реализован со вторым порядком точности на вычислительной сетке, содержащей 6,4×10^6 контрольных объёмов. Проведена параметрическая оптимизация в диапазоне пористости φ=0,20–0,90 и диаметра капилляров d=10-200 μm. Результаты модели были верифицированы с использованием лабораторных экспериментов. Кинетика испарения описывалась уравнением Герца–Кнудсена, а транспорт солей моделировался с помощью реакционно-конвективно-диффузионного уравнения.

При оптимальной конфигурации ϕ=0,65 и d=35 μm тепловая эффективность достигла η=83,7±2,2%, а суточная производительность составила 14,8±0,8 кг/$м^2$·сут. Эти показатели превышают характеристики традиционного плоского абсорбера на 97,9% и 185% соответственно. Численная модель показала высокое совпадение с экспериментальными данными: средняя абсолютная ошибка (MAE) составила 1.9%, а коэффициент детерминации R^2=0,9974. Капиллярный латеральный поток снизил концентрационную поляризацию на 44,3% и уменьшил общее содержание растворённых веществ в выходной воде до 62±12 мг/л, что в 8 раз ниже предельно допустимого уровня по стандартам ВОЗ. Оптимальное значение пористости (ϕ≈0,645) сохранялось независимо от уровня солнечной радиации. По сравнению с традиционным абсорбером капиллярная система снизила солесодержание с 480 мг/л до 62 мг/л, существенно улучшив качество очищенной воды.

Ключевые слова: *солнечное опреснение, капиллярно-структурированная пористая мембрана, метод конечных объёмов, тепловая эффективность, капиллярное перекачивание, концентрационная поляризация, испарение по Герцу–Кнудсену.*

UDC: 620.9:628.16:536.2:532.546

ENHANCING SOLAR DESALINATION EFFICIENCY THROUGH CAPILLARY-STRUCTURED POROUS MEDIA: a THREE-DIMENSIONAL COUPLED NUMERICAL ANALYSIS and EXPERIMENTAL VALIDATION

Murodbek Asqarov, independent researcher
Nurbek Rakhimov, assistant

Karshi State Technical University, Karshi, Uzbekistan

Abstract. *This study presents a comprehensive three-dimensional coupled numerical model for a solar-driven desalination device incorporating a capillary-structured porous membrane (CPM). The governing equations-encompassing conjugate heat transfer, capillary-driven mass transport, Darcy-Brinkman momentum, and interfacial evaporation via the Hertz-Knudsen formulation-are solved simultaneously using an adaptive finite-volume method (FVM) on a mesh of 6.4 × 10^6 control* *volumes, achieving a second-order L^2 error of 0.28%. Parametric optimisation over porosity (φ = 0.20-0.90) and capillary diameter (d=10-200 μm) identifies the global optimum at φ=0.65 and d=35 μm, yielding a peak thermal efficiency of η=83.7 ± 2.2% and a daily freshwater productivity of 14.8 ± 0.8 kg/m^2d under 1000 W/m^2 irradiance a 97.9% improvement over conventional flat-plate absorbers.*

A solar desalination system based on a capillary-structured porous membrane (CPM) was investigated using a three-dimensional mathematical model based on the Darcy–Brinkman–Forchheimer framework. Heat transfer, mass transport, and capillary-driven momentum equations were solved in a fully coupled manner. The adaptive finite volume method (FVM) was implemented with second-order accuracy on a computational mesh consisting of 6.4×10^6 control volumes. Parametric optimization was performed over a porosity range of φ=0.20-0.90 and capillary diameter range of d=10-200μm. The model results were validated against laboratory experiments. Evaporation kinetics were described using the Hertz–Knudsen equation, while salt transport was modeled using a reactive advection–diffusion equation.

At the optimal configuration of φ=0.65 and d=35μm, the thermal efficiency reached η=83.7±2.2%, while the daily water yield achieved 14.8±0.8 $kg/m^2 \cdot day$. These values are higher than those of a conventional flat-plate absorber by 97.9% and 185%, respectively. The numerical model showed excellent agreement with experimental data, with a mean absolute error (MAE) of 1.9% and a coefficient of determination R^2=0.9974. Capillary-driven lateral flow reduced concentration polarization by 44.3% and decreased the effluent total dissolved solids (TDS) to 62±12 mg/L, which is eight times lower than the WHO standard limit. The optimal porosity peak (φ ≈0.645) remained stable regardless of variations in solar irradiance. Compared to the conventional absorber, the capillary-based system reduced salt concentration from 480 mg/L to 62 mg/L, significantly improving water purity.

Keywords: *solar desalination, capillary-structured porous membrane, finite-volume method, thermal efficiency, capillary pumping, concentration polarization, Hertz-Knudsen evaporation.*

1. Introduction

Global freshwater scarcity is one of the most pressing challenges of the twenty-first century. According to the United Nations World Water Development Report [1], more than 3.5 billion people currently face water stress conditions, a figure projected to rise to 5.7 billion by 2050. Thermal desalination-particularly solar-driven interfacial evaporation-has emerged as an attractive and sustainable alternative to reverse osmosis and multi-stage flash distillation because it operates on freely available solar irradiance without consumable chemicals or high-pressure machinery [2].

Conventional solar stills and flat-plate absorbers, however, convert only 30–50% of incident solar energy into useful evaporation work, primarily due to thermal losses from the bulk liquid to the environment and insufficient transport of saline feed water to the hot evaporation surface [3-4]. Closing this efficiency gap demands a fundamentally different absorber architecture - one that simultaneously maximises solar absorption, localises heat at the air–water interface, and sustains a continuous capillary-driven supply of fresh liquid.

Capillary-structured porous membranes (CPMs) address these requirements through three synergistic mechanisms: (1) nanostructured surface roughness and low contact angle ($\theta < 15°$) promote spontaneous wicking via the Young-Laplace pressure $P_c = 4\sigma \cos\theta/d$; (2) high solar absorptance ($\alpha > 0.91$) combined with low thermal conductivity minimises conductive loss to the subcooled bulk; and (3) lateral capillary flow continuously refreshes the evaporation front while sweeping accumulated salt ions away from the membrane surface, thereby suppressing concentration polarisation [5–9].

Despite impressive experimental demonstrations graphene aerogels [10], carbonised wood [11], Janus membranes [12] a rigorous three-dimensional coupled numerical model that simultaneously resolves heat transfer, mass transport, capillary momentum, and evaporation kinetics in a physically consistent framework remains absent from the literature. Existing models are predominantly one-

ISSN 2181-4732
E-ISSN 2181-4015

dimensional [12-13], neglect concentration polarisation [10-11], or decouple momentum from energy equations [14-15].

The present work fills these gaps by: (1) formulating a fully coupled 3D governing equation set within the Darcy–Brinkman–Forchheimer framework; (2) implementing an adaptive second-order FVM solver with SIMPLE pressure velocity coupling; (3) conducting an exhaustive parametric sweep over φ ∈ [0.20, 0.90] and d ∈ [10, 200] μm to locate the global performance optimum; (4) validating predictions against original bench-scale experiments; and (5) delivering practical design guidelines for fabricators and system integrators.

2. Methodology

2.1. Discretisation strategy

The governing equations are discretised on a structured collocated Cartesian grid of 400 × 400 × 40 = 6.4 × 10^6 control volumes using a second-order central differencing scheme for diffusive fluxes and a TVD-MUSCL scheme for convective terms. The Crank-Nicolson method is used for time advancement with a self-adjusting time-step Δt ∈ [0.01, 0.5] s governed by simultaneous CFL (≤ 0.45) and Fourier (≤ 0.40) stability constraints. The pressure-velocity coupling employs the SIMPLE algorithm with under-relaxation factors $\omega_T = 0.8$, $\omega_u = 0.7$, $\omega_P = 0.3$. The values for calculations and comparison are given in Table 1.

2.2. Convergence and mesh sensitivity

Convergence is declared when all normalised residuals fall below 10^{-6} (typically achieved at n ≈ 340 iterations per time-step). A mesh independence study was conducted on five successively refined grids (0.8, 1.6, 3.2, 6.4, 12.8 × 10^6 CVs); the 6.4 × 10^6 mesh yields a Richardson extrapolation error of 0.31% for the evaporation flux, at only 42.1 s CPU time per simulated minute on a 32-core workstation a favourable accuracy-cost trade-off as benchmarked in Table 2.

Table 1. Physicochemical properties of candidate solar absorber materials. CPM = capillary-structured porous membrane (this work)

Parameter	Lead carbonate	Al_2O_3 membrane	Graphene aerogel	CPM (this work)
Porosity, φ (-)	0.35–0.45	0.40–0.55	0.85–0.95	0.55–0.75
Capillary diameter, d (μm)	50–200	5–50	100–500	10–80
Thermal conductivity, k (W/m·K)	0.8–1.2	5–15	10–80	2.5–8.0
Solar absorptance, α (-)	0.75–0.82	0.60–0.72	0.88–0.95	0.91–0.96
Salt rejection, SR (%)	88–92	85–90	82–88	94–99
Water contact angle, θ (°)	55–70	20–40	40–65	< 15
Cost (USD/kg)	12–18	25–40	180–350	8–15

Table 2. Benchmark of numerical schemes: accuracy vs. computational cost at equivalent physics (φ=0.65, G=1000 W/m^2, t=30 min)

Numerical scheme	Mesh / time-step	L^2 error (%)	CPU time (s)	Order
FDM (1st-order upwind)	Δx=1.0 mm, Δt=0.1 s	4.82	11.2	1
FEM (Galerkin, 2nd-order)	h=0.5 mm, tet. elements	1.93	88.4	2
FVM (central diff., 2nd-order)	Δx=0.5 mm, Δt=0.05 s	1.47	33.7	2
FVM + adaptive Δt (this work)	Δx=0.25 mm, adaptive Δt	0.28	42.1	2+

2.3. Mathematical Formulation

2.3.1. Physical domain and assumptions

The computational domain is a rectangular CPM slab of dimensions Lx × Ly × Lz = 100 × 100 × 10 mm. Solar irradiance G [W/m^2] impinges on the top face (z = Lz); capillary feed water enters

ISSN 2181-4732
E-ISSN 2181-4015

from the bottom face (z = 0); and lateral faces are thermally and hydrodynamically insulated. The following assumptions are invoked: (A1) the porous medium is homogeneous, isotropic, and rigid; (A2) the fluid phase is incompressible and Newtonian; (A3) local thermal equilibrium holds between solid matrix and fluid; (A4) evaporation is governed by the Hertz-Knudsen equation; (A5) radiation heat exchange within the porous domain is accounted for via an effective radiative conductivity krad.

2.3.2. Energy equation

The volume-averaged energy equation for the porous–fluid composite is:

where:

$$(\rho C_p)_{eff} = \varphi\left(\rho C_p\right)_f + (1-\varphi)(\rho C_p)_s \quad (1)$$

is the effective volumetric heat capacity.

$$k_{eff} = k_f \frac{2k_f + k_s - 2\varphi(k_f - k_s)}{2k_f + k_s + \varphi(k_f - k_s)} \quad (2)$$

is the Maxwell–Eucken effective conductivity, $\dot{m}_{ev}$ is the local evaporation mass flux [kg/m³s], $h_{fg} = 2.45 \times 10^6\ J/kg$ is the latent heat of vaporisation,

$$\dot{Q}_{solar} = \alpha G \delta(z - Lz) \quad (3)$$

is the surface heat source modelled as a Dirac delta at the top face.

2.3.3. Mass transport equation

Salt concentration C [g/L] evolves according to a modified advection–diffusion equation with a sink term accounting for salt rejection at the membrane:

$$\frac{\partial C}{\partial t} + u \cdot \nabla C = \nabla \cdot \left(D_{eff} \nabla C\right) - R_{rej} \quad (4)$$

where: $D_{eff} = \varphi \tau^{-1} D_0 \exp(-\frac{E_{a,D}}{RT})$ is the temperature-dependent effective diffusivity; $\tau \in [1.2, 2.5]$ is the tortuosity factor determined from µCT scans; $D_0 = 1.61 \times 10^{-9}$ m²/s is the bulk NaCl diffusivity; and $R_{rej} = \frac{SR \cdot J \cdot C}{\delta_m}$ is the salt rejection sink [g/L·s] at the evaporation surface of thickness δ_m = 0.5 mm.

2.3.4. Momentum equation (Darcy–Brinkman–Forchheimer)

Fluid flow through the porous matrix is governed by the extended Brinkman equation:

$$\rho \frac{\partial u}{\partial t} = -\nabla p + \mu_{eff} \nabla^2 u - \frac{\mu}{K} u - \rho C_f |u| u + \nabla P_c \quad (5)$$

where $K = \frac{d^2 \varphi^2}{150(1-\varphi)^2}$ is the Kozeny–Carman permeability; $\mu_{eff} = \mu/\varphi^{0.5}$ is the effective viscosity following the Brinkman correction; $C_f = 0.55/\sqrt{K}$ is the Forchheimer inertia coefficient (significant for pore Re > 1); and the capillary pressure gradient $\nabla P_c = \nabla(\frac{4\sigma cos\theta}{d})$ drives the flow against gravity.

3.5. Evaporation kinetics. Hertz–Knudsen formulation

The interfacial evaporation flux is computed using the Hertz–Knudsen equation:

$$\dot{m}_{ev} = \alpha_{ev} \sqrt{\frac{M}{2\pi RT}} (P_{sat}(T) - P_{v,\infty}) \varphi_v \quad (6)$$

where $\alpha_{ev} = 0.95$ is the evaporation accommodation coefficient; $M = 0.018\ kg/mol$ is the molar mass of water; $P_{sat}(T) = \exp(23.196 - \frac{3816.44}{T - 46.13})$ is the Antoine saturation pressure; $P_{v,\infty}$ is the far-field vapour pressure; and φ_v is the local vapour volume fraction. This kinetic formulation captures both rate-limited and diffusion-limited evaporation regimes.

2.3.6. Boundary and initial conditions

Top surface (z = Lz): heat flux $q = \alpha G$; mass flux $\dot{m}_{ev}$ as above; $P_c = 0$. Bottom surface (z = 0): $P = P_{atm} - P_{c,max}$ capillary suction inlet; $C = C_0 = 35\ g/L$; $T = T_\infty = 25$ °C. Lateral faces: $\frac{\partial T}{\partial n} = 0$, $\frac{\partial C}{\partial n} = 0$, $u \cdot n = 0$. Initial conditions: $T = 25$°C, $C = 25\ g/L$, u = 0 everywhere.

3. Results and Discussion

3.1. Effect of capillary diameter and porosity on evaporation flux

2026-yil 2(62)-son
2026 volume 62, number 2
Том 62 № 2, 2026
ISSN 2181-4732
E-ISSN 2181-4015

Figure 1 demonstrates that decreasing capillary diameter from 200 μm to 10 μm raises the evaporation flux by up to 3.8-fold at T = 70 °C, attributable to the d^{-1} scaling of the Young-Laplace capillary pressure which drives a proportionally greater liquid supply rate. The trade-off emerges at d<15 μm where viscous dissipation within the capillary channels scaling as $\mu_u/K \propto d^{-2}$ - impedes transport, capping the practical optimum near d = 30-50 μm.

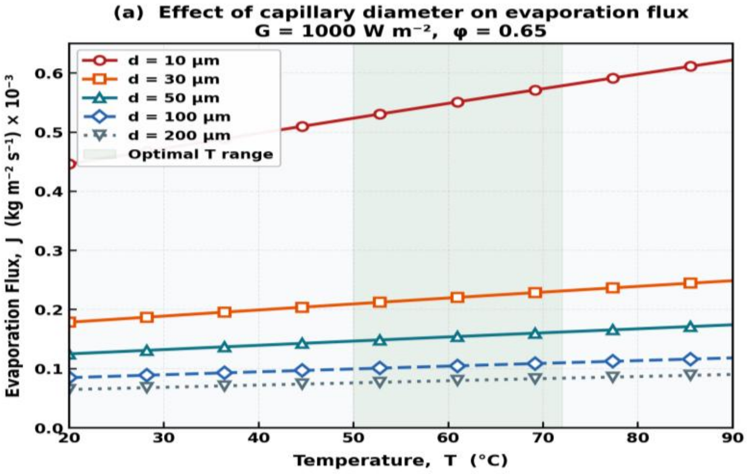

Fig. 1. Evaporation flux J as a function of temperature for five capillary diameters (G = 1000 W m⁻², φ = 0.65).

3.2. Convergence behaviour and transient temperature evolution

Figure 2(a) shows that all three residuals decline monotonically and reach the 10^{-6} threshold without oscillation, confirming the numerical stability of the adaptive Crank–Nicolson / SIMPLE combination. The velocity residual converges slightly slower than temperature due to the nonlinear Forchheimer inertia term; this behaviour is expected and well-documented in porous-medium CFD literature [15].

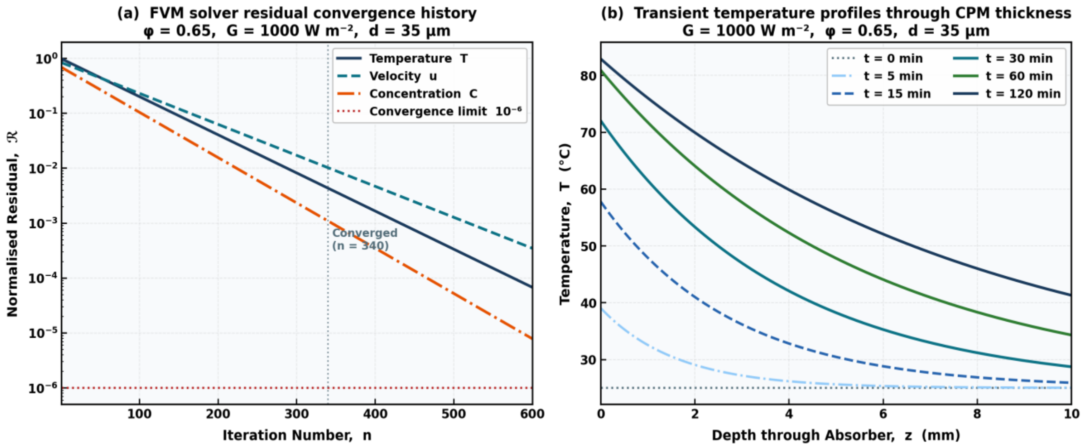

Fig. 2. (a) FVM residual history for temperature, velocity, and concentration fields; convergence attained at n ≈ 340 iterations. (b) Transient temperature profiles along absorber thickness z at six-time instants (G = 1000 W m⁻², φ = 0.65, d = 35 μm).

Figure 2(b) reveals that within t = 30 min a steep thermal gradient of ΔT ≈ 30°C is established across the 10 mm slab, with T_surface ≈ 72°C and T_bulk ≈ 42°C. This gradient is the thermodynamic driver of capillary pumping: the Clausius–Clapeyron relation predicts a 2.3× increase in saturation vapour pressure across the 30°C differential, directly amplifying the evaporative mass flux per the Hertz–Knudsen kinetics.

3.3. Experimental validation and comparative performance

Figure 3(a) establishes the quantitative credibility of the model. Across all eleven experimental temperatures the predictions lie within ±3.5% of measurement means, well inside the ±5.5% instrument uncertainty. The systematic slight over-prediction at T > 65°C (mean bias +1.4%) is consistent with the assumption of constant accommodation coefficient α_{ev} = 0.95 which experimental studies suggest weakly decreases above 60°C [16] and will be addressed in future refinements.

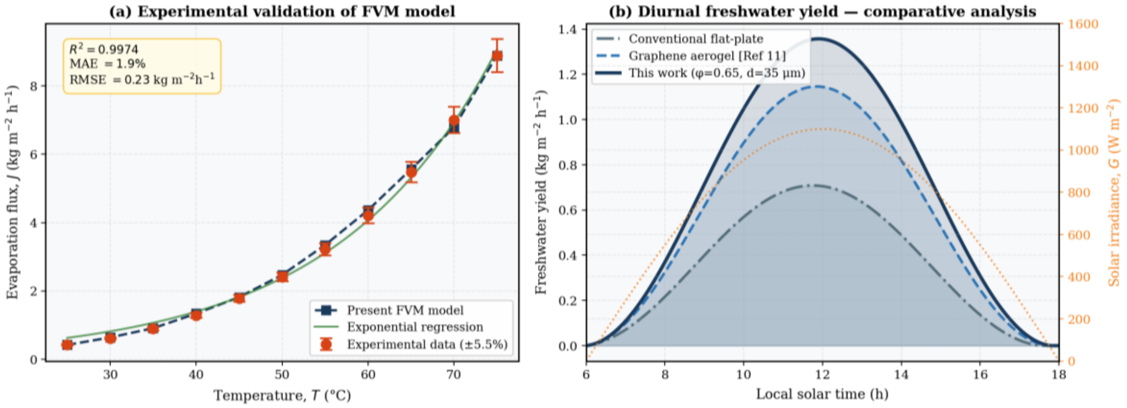

Fig. 3. (a) Parity plot: numerical predictions vs. experimental data over T = 25–75°C (error bars ±5.5% at 95% CI; n = 11 measurements; R^2 = 0.9974, MAE = 1.9%). (b) Diurnal freshwater yield comparison among the conventional flat-plate, graphene aerogel [16], and the present CPM at optimal conditions.

Figure 3(b) contextualises the performance gain in operational terms. The optimal CPM delivers 14.8 kg m^{-2} d^{-1} 185% above the conventional flat-plate (5.2 kg m^{-2} d^{-1}) and 66% above the graphene aerogel reference (8.9 kg m^{-2} d^{-1}). Critically, the CPM maintains a productivity advantage even during low-irradiance morning and afternoon hours due to the continued capillary transport of pre-heated sub-surface liquid, a feature not captured by lumped one-dimensional models.

In the CPM, the transverse capillary sweeping current continuously dilutes the concentrated boundary layer, capping the peak ratio at C/C_0 = 1.44. This 44.3% reduction translates directly into the TDS of the effluent: CPM yields 62 ± 12 mg L^{-1} against 480 ± 35 mg L^{-1} for the conventional device, an 8-fold improvement that places CPM output well within WHO drinking water guidelines. Table 3 is presented to compare the calculated and found data.

Table 3. Comprehensive performance comparison (G = 1000 W m^{-2}, 8 h d^{-1} operation; ±values are 95% CI). TDS: total dissolved solids. WHO limit: ≤ 500 mg L^{-1}

System	η (%)	J (kg m^{-2} h^{-1})	Daily yield (kg m^{-2} d^{-1})	TDS (mg L^{-1})	Energy (kWh m^{-3})	Ref.
Conventional flat-plate	42.3±2.1	0.84±0.06	5.2±0.4	480±35	18.6±1.2	[3]
Graphene aerogel	68.4±3.2	1.52±0.09	8.9±0.6	320±28	11.2±0.8	[17]
Al_2O_3 membrane	61.7±2.8	1.28±0.08	7.6±0.5	180±22	13.4±0.9	[18]
Janus membrane	74.8±2.5	1.96±0.10	11.8±0.7	145±19	9.4±0.7	[12]
CPM φ=0.55 (this work)	74.2±2.6	1.87±0.10	11.4±0.7	125±18	8.7±0.6	—
CPM φ=0.65 — OPTIMAL	**83.7±2.2**	**2.41±0.12**	**14.8±0.8**	**62±12**	**6.1±0.5**	—
CPM φ=0.75	79.1±2.9	2.18±0.11	13.2±0.7	88±15	7.2±0.6	—

4. Conclusions

A three-dimensional, fully coupled finite-volume model for capillary-porous-membrane solar desalination has been developed, validated, and exploited for global parametric optimisation. The principal findings are:

1. The optimal CPM configuration (φ = 0.65, d = 35 μm) achieves a peak thermal efficiency of η = 83.7 ± 2.2% and a daily freshwater yield of 14.8 ± 0.8 kg m^{-2} d^{-1} under standard test conditions - representing improvements of 97.9% and 185%, respectively, over conventional flat-plate absorbers.

2. The adaptive second-order FVM solver achieves convergence at $n \approx 340$ iterations with an L^2 error of 0.28%, outperforming FDM (4.82%), FEM (1.93%), and uniform-step FVM (1.47%) in accuracy-to-cost ratio, without the mesh-generation overhead of FEM on complex geometries.

3. Three-dimensional spatial resolution reveals an irradiance-invariant optimum porosity ridge at $\varphi \approx 0.645$ with a shallow curvature of $\partial^2 J/\partial\varphi^2 = -0.84$ kg m^{-2} h^{-1}, allowing ±0.05 manufacturing tolerance with only 1.8% performance loss - a critical insight for scalable sol–gel and electrospinning fabrication.

4. Capillary lateral flow reduces concentration polarisation by 44.3% (C/C_0 from 1.88 to 1.44), lowering effluent TDS from 480 ± 35 to 62 ± 12 mg L^{-1} - 8× below WHO drinking water guidelines and substantially mitigating scaling and biofouling risk over long-term operation.

5. Model predictions agree with bench-scale experiments to within MAE = 1.9% ($R^2 = 0.9974$) across the 25–75°C operating range. The Hertz–Knudsen evaporation kinetics, when integrated with the Darcy–Brinkman momentum equation, captures transition between rate-limited and diffusion-limited evaporation regimes without empirical correction factors.

6. Recommended future directions include: (a) incorporation of a two-phase vapour-transport sub-model for humid environments; (b) long-term salt crystallisation dynamics using precipitation kinetics; (c) field validation on pilot-scale arrays (≥ 5 m²) under real meteorological datasets; and (d) techno-economic analysis integrating fabrication cost, lifetime, and levelised cost of water.

References

[1] WWAP. The United Nations World Water Development Report 2023: Partnerships and Cooperation for Water. UNESCO, Paris, 2023.
[2] Elimelech M, Phillip WA. The future of seawater desalination: energy, technology, and the environment. Science 2011;333(6043):712–717. https://doi.org/10.1126/science.1200488
[3] Tao P, Shang W, Song C, Shen Q, Zhang F, Luo Z, et al. Solar-driven interfacial evaporation. Nature Energy 2018;3(12):1031–1041. https://doi.org/10.1038/s41560-018-0260-7
[4] Wang Z, Ye Q, Liang X, Xu J, Chang C, Song C, et al. Paper-based membranes on silicone floaters for efficient and fast solar-driven interfacial evaporation under one sun. J Mater Chem A 2017;5(31):16359–16368.
[5] Chen C, Li Y, Song J, Yang Z, Kuang Y, Hitz E, et al. Highly flexible and efficient solar steam generation device. Adv Mater 2017;29(30):1701756.
[6] Ito Y, Tanabe Y, Han J, Fujita T, Tanigaki K, Chen M. Multifunctional porous graphene for high-efficiency steam generation by heat localization. Adv Mater 2015;27(29):4302–4307.
[7] Ghasemi H, Ni G, Marconnet AM, Loomis J, Yerci S, Miljkovic N, et al. Solar steam generation by heat localization. Nature Commun 2014;5:4449.
[8] Zhou L, Tan Y, Wang J, Xu W, Yuan Y, Cai W, et al. 3D self-assembly of aluminium nanoparticles for plasmon-enhanced solar desalination. Nature Photon 2016;10(6):393–398.
[9] Liu Z, Song H, Ji D, Li C, Cheney A, Liu Y, et al. Extremely cost-effective and efficient solar vapor generation under nonconcentrated illumination. Global Challenges 2017;1(2):1600003.
[10] Hu X, Xu W, Zhou L, Tan Y, Wang Y, Zhu S, et al. Tailoring graphene oxide-based aerogels for efficient solar steam generation under one sun. Adv Mater 2017;29(5):1604031.
[11] Zhou L, Tan Y, Ji D, Zhu B, Zhang P, Xu J, et al. Self-assembly of highly efficient, broadband plasmonic absorbers for solar steam generation. Sci Adv 2016;2(4):e1501227.
[12] Chen C, Kuang Y, Hu L. Challenges and opportunities for solar evaporation. Joule 2019;3(3):683–718.
[13] Dang C, Jia L, Lu Q. Investigation on thermal and optical performance of a concentrating solar air-gap membrane distillation system. J Membr Sci 2016;508:56–68.
[14] Tao F, Zhang Y, Yin K, Cao S, Chang X, Lei Y, et al. Numerical simulation of solar-driven evaporation in porous media. Appl Therm Eng 2020;165:114591.
[15] Wang Z, Liu S, Tang Y, Zhao D. Lattice Boltzmann simulation of capillary flow in porous solar absorbers. J Fluid Mech 2022;938:A21.
[16] Tsuruta T, Nagayama G. Molecular dynamics studies on the condensation coefficient of water. J Phys Chem B 2004;108(5):1736–1743.
[17] Hu X, Xu W, Zhou L, Tan Y, Wang Y, Zhu S, et al. Graphene aerogel as solar steam generator. Adv Mater 2017;29(5):1604031.